Custom Phase Space Reconstruction Image-Driven Fault Diagnosis for PMSM Under Few-Labeled Samples

Jinping Xie, Xiaofei Zhang, *Senior Member, IEEE*, Derong Luo, Guojun Qin, and Fengqin Huang

***Abstract*—The existing intelligent fault diagnosis methods for motors mainly focus on the supervised learning of 1-D signals, which ignores the global features of the signal and requires large training samples of labeled data. For this reason, this article proposes a custom double-sided phase space reconstruction (CDPSR) image-driven fault diagnosis method for permanent magnet synchronous motor (PMSM) under few-labeled samples. To reveal 2-D features in the signal, a CDPSR method is proposed to convert the fault signal into data images. The two-parallel diagnostic framework is designed, which includes 1) two semisupervised stacked autoencoders for image feature extraction and primary classification and 2) the weighted decision fusion layer to output the final diagnosis result. The extensive diagnostic results on the experimental platform verify the effectiveness of the proposed method for PMSM fault diagnosis.**

***Index Terms*—Data-driven diagnostic method, double-sided data image, permanent magnet synchronous motor (PMSM), semisupervised learning.**

I. Introduction

PERMANENT magnet synchronous motor (PMSM) and its related application equipment play a vital role in industrial production, being essential [1]. As a vital part of the power system, various faults of PMSM during the entire service period may lead to serious safety accidents. Therefore, the investigation of fault diagnosis technology for PMSM is of great significance.

The rotary motor faults usually include rotor faults, stator faults, and bearing faults (BFs) [2]. The rotor fault of PMSM is mainly a permanent magnet fault, and the stator fault is a short circuit fault. With the increasing development of artificial intelligence technology, the data-driven method for motor fault diagnosis has become a research hotspot [3], which mines fault features by establishing statistical models of motor state signals. Several state signals such as induced electromotive force [4], [5], current and voltage [6], [7], magnetic flux [8], [9], [10], and vibration [11], [12] have been proven to be effective in fault diagnosis. The current and voltage signals were preprocessed by Hilbert–Huang transform and combined with the convolution neural network for fault diagnosis [6]. Song et al. [8] used the air-gap flux after complex continuous wavelet transform (CWT) as the input of the random forest classifier to diagnose demagnetization faults. Wang et al. [11] performed the short-time Fourier transform and a wavelet transform on the vibration signal for BF diagnosis. However, the fault feature extraction of the previous methods is based on the artificial feature extraction of 1-D signals, which generally requires complex signal preprocessing to explore the 1-D features, ignoring the 2-D features or higher dimensions features. Deep learning around neural networks has been developed based on machine learning and is widely used in image classification and recognition. Converting the fault signal into a suitable image guides a new direction for fault diagnosis of rotary machinery, which is more conducive to fault diagnosis [13]. Currently, image-based fault diagnosis is mainly divided into directly measured images and signal-converted data images. Choudhary et al. [14] and Shao et al. [15] conducted fault diagnosis of bearings by measuring the infrared thermal images. Tran et al. [16] adopted the time–frequency characteristic images of vibration signals to diagnose bearing and rotor faults. However, the infrared imager is difficult to install and high cost, and the time–frequency image is susceptible to interference from noise. To this end, the fault signal was converted into an symmetrized dot pattern (SDP) image for fault diagnosis of PMSM and induction motor in [13] and [17], which proved the effectiveness of SDP image in fault diagnosis. However, according to the principle of SDP image, only one pair of bridge arms in the SDP image is constructed from the original data, and the rest are cyclic recurrences, which have repetitive information that increases the computational cost.

In practical industrial applications, the fault categories of industrial data are usually unknown, and it is difficult and costly to label the data accurately and completely [18]. Despite the rapid progress in data-driven intelligent fault diagnosis of PMSM, most of the existing methods focus on supervised learning, and a large amount of labeled data is required to train the model. To address this practical application problem, the

Manuscript received 12 May 2023; revised 1 September 2023; accepted 12 November 2023. Date of publication 15 November 2023; date of current version 22 December 2023. This work was supported in part by the National Key Research and Development Program of China under Grant 2022YFF0608700, in part by the National Science Foundation of China under Grant 52077064, and in part by the Key Research and Development Program of Hunan under Grant 2023GK2006. Recommended for publication by Associate Editor A. Yazdani. *(Corresponding authors: Xiaofei Zhang; Derong Luo.)*

The authors are with the College of Electrical and Information Engineering, Hunan University, Changsha 410082, China (e-mail: xiejinping@hnu.edu.cn; zhangxiaofei@hnu.edu.cn; hdldr@hnu.edu.cn; qgj@nudt.edu.cn; huangfengqin@hnu.edu.cn).

Color versions of one or more figures in this article are available at https://doi.org/10.1109/TPEL.2023.3332959.

Digital Object Identifier 10.1109/TPEL.2023.3332959

semisupervised approaches that combine labeled and unlabeled samples are being studied. The goal of semisupervised training methods is to effectively utilize unlabeled data to improve diagnostic performance by smoothing the classification function with clustering assumptions under a small amount of labeled data [19]. At present, most of the motor fault diagnosis work related to semisupervised learning is based on deep neural network methods. For example, Zhang et al. [20] built a deep prototype network employing limited labeled samples to make pseudolabels for unlabeled data, enabling semisupervised learning of fault diagnosis models. Zhang et al. [21] proposed a deep adversarial semisupervised approach that leverages a prototype learning network to tackle BF diagnosis. To make effective use of unmarked multisensor signals for mechanical fault detection, Nie and Xie [22] proposed a two-stage semisupervised learning method. Neural networks that have several hidden layers are beneficial for addressing the identification of complex scenarios. Nevertheless, the corresponding networks are difficult to construct in practice. The autoencoder can realize the layer-by-layer training of the hidden layers, and adjust the required number of hidden layers according to the actual data, which effectively simplifies the training process of the neural network. Semisupervised fault diagnosis methods based on stacked autoencoders (SAE) have been gradually studied. Liu et al. [23] and Wang et al. [24] applied semisupervised SAE (S-SAE) to the detections of BFs and rail foreign objects, respectively. Up to now, there are a few studies on semisupervised learning in the fault diagnosis field, and mainly use deep neural networks that need to train multiple hidden layers at a time.

To address the above-mentioned issues, this article proposes a custom phase space reconstruction (PSR) image-driven fault diagnosis method for PMSM under few-labeled samples. First, the magnetic leakage signal is chosen as the fault signal, and a custom double-sided PSR (CDPSR) technology is designed to convert the fault signals into 2-D images (CDPSR images). Then, a parallel semisupervised stacked autoencoder (PS-SAE) diagnostic framework is designed. The PS-SAE consists of two parts. 1) Two S-SAEs are used for feature extraction and primary classification of CDPSR images. 2) The two primary classification results are fused to achieve the final fault diagnosis through the weighted decision layer fusion method. Finally, an experimental platform equipped with five kinds of faulty PMSMs is established for experimental validation, and the results indicate the effectiveness of the proposed method. In summary, the main contributions of this article are as follows.

1) A new framework for intelligent fault diagnosis of PMSM under few-labeled samples is proposed. The CDPSR image of magnetic leakage signals is constructed to characterize the health of PMSMs.
2) It originally proposed a data image reconstruction method based on CDPSR, which transforms the magnetic leakage signal into a CDPSR image. The 2-D global features hidden in faulty signals are intuitively revealed.
3) A novel PS-SAE is designed for PMSM fault diagnosis, simplifying the training process and reducing individual errors through layer-by-layer semisupervised training and decision-level fusion strategy.

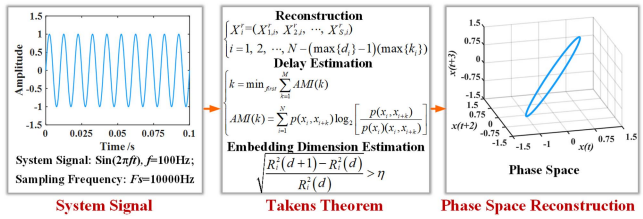

Fig. 1. Classical PSR of sinusoidal signals.

The rest of this article is organized as follows. Section II illustrates the classical PSR. Section III shows the details of the proposed method. Section IV demonstrates the introduction of the experimental platform, the experimental verification, and the analysis. Finally, Section V concludes this article.

II. Classical Phase Space Reconstruction

The PSR technology is utilized to transform the time series data of nonlinear systems into state vectors, effectively representing system characteristics, which simplifies the analysis of nonlinear systems [25], [26]. The PSR holds that the time series that records the long-term evolution of the system includes the evolution characteristics of the system. The commonly used PSR method is the Takens delayed embedding theorem, also known as the Takens theorem. The theorem treats the time series at different fixed delay points as a new series of different dimensions and uses them to reconstruct the equivalent state space of the nonlinear system.

The key parameters of Takens's theorem are delay (k) and embedding dimension (d). The average mutual information (AMI) of the time series at various delays is calculated and the first local minimum value of AMI is selected as the parameter k. The AMI can be expressed as [26]

$$\begin{cases} k = \min_{\text{first}} \sum_{k=1}^{M} \text{AMI}(k) \\ \text{AMI}(k) = \sum_{i=1}^{N} p(x_i, x_{i+k}) \log_2 \left[\dfrac{p(x_i, x_{i+k})}{p(x_i)(x_i, x_{i+k})} \right] \end{cases} \tag{1}$$

where k takes values sequentially from 1 to the setting maximum delay. The false nearest neighbor (FNN) algorithm is commonly employed to calculate d. It determines whether the proportion of points satisfying the FNN reaches the setting proportion in the phase space of different dimensions, and uses the phase space with the smallest dimension that satisfies the condition as the reconstructed phase space. The FNN of point i of time series in d-dimensional space can be written as [26]

$$\sqrt{\frac{R_i^2(d+1) - R_i^2(d)}{R_i^2(d)}} > \eta \tag{2}$$

where $R_i^2(d)$ is the distance calculation and η is the threshold. Assume a signal of a nonlinear system is a sinusoidal signal $(\sin(2\pi ft), f = 100\ \text{Hz})$, the time series is formed by sampling at a frequency of 10 kHz. According to Takens's theorem, the parameters of its PSR are $k = 2$ and $d = 3$. Fig. 1 shows the PSR of this signal.

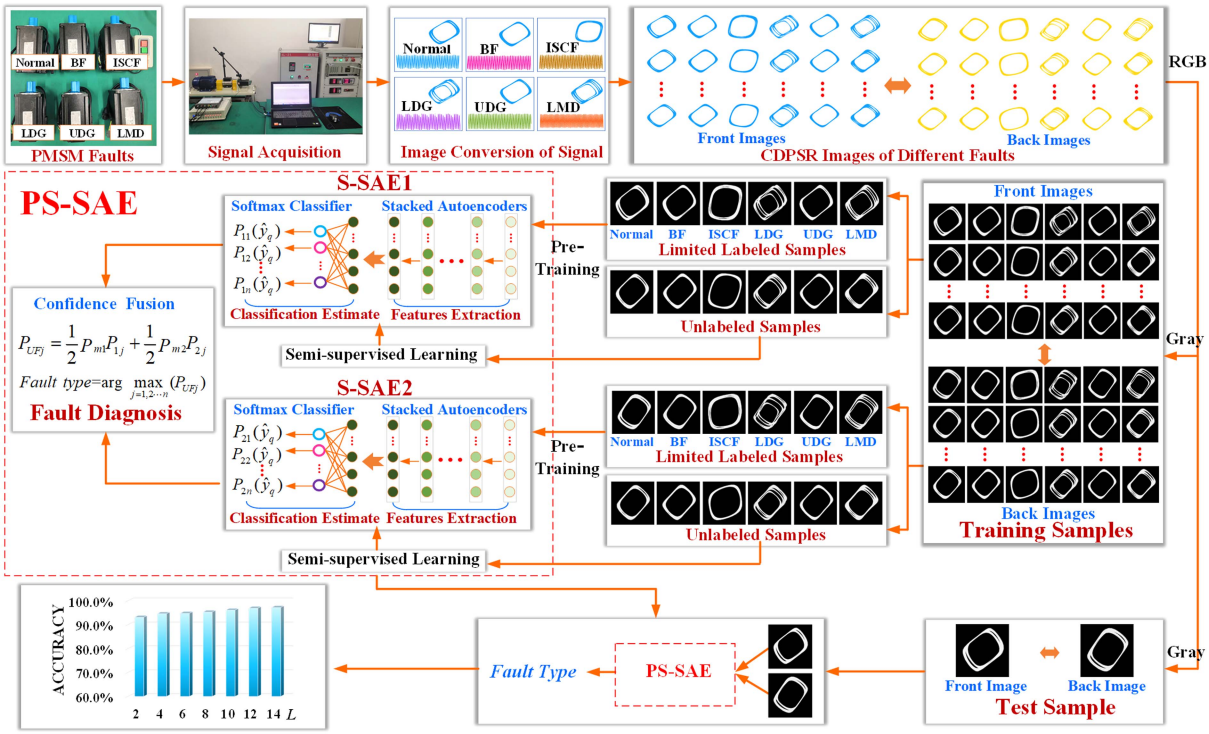

Fig. 2. Diagnostic framework of the proposed method.

III. Proposed Method

This article designs an intelligent fault diagnosis method for PMSM, which mainly concludes CDPSR images and a two-parallel diagnostic framework. The framework is shown in Fig. 2.

A. CDPSR Method

As mentioned earlier, the fault signal to image conversion will visually present the 2-D global fault features. From Section II, it can be observed that the PSR can reconstruct the signal into phase space trajectories with certain regularity. To simplify the PSR of motor and facilitate fault diagnosis, the CDPSR method is proposed motivated by classical PSR and visual image knowledge, which converts 1-D fault signals into data images.

1) Embedding Dimension: According to the principle of PSR, the signal of a nonlinear system can be reconstructed in phase space of different dimensions. Therefore, specific judgment conditions can be formulated to select appropriate delay and embedding dimensions for specific research questions. To represent the 2-D fault features, this article fixes $d = 2$ to reconstruct 2-D phase space trajectory, which consists of two 1-D phase space vectors.

2) Delay: The AMI judgment method of classical PSR only focuses on the PSR of individual systems without considering the differences between systems. Furthermore, the study found that the classical PSR method assigns different delays to the fault signals of different operating conditions under the identical fault so that the difference between the images is large which is not conducive to fault diagnosis.

To tackle the above-mentioned problems, this article presents a delay determination method that applies to fault diagnosis. First, to enhance the adaptability of images of identical faults under diverse working conditions, all systems take the identical fixed delay k. The average normalization mutual information (ANMI) of images between different systems is compared and calculated under different delays, and the first local minimum value is taken as k. The calculation can be expressed as

$$\begin{cases} k = \min_{\text{first}} \sum_{k=1}^{N} \text{ANMI}(k) \\ \text{ANMI}(k) = \frac{1}{n} \sum_{j=1}^{n} \text{NMI}(I_{kj_1}, I_{kj_2}); j_1 \neq j_2 \\ \text{NMI}(I_{kj_1}, I_{kj_2}) = \frac{H(I_{kj_1}) + H(I_{kj_2})}{H(I_{kj_1}, I_{kj_2})} \end{cases} \tag{3}$$

where I_{kj_1} and I_{kj_2} are the phase space images of two different faulty motors ($j_1 \text{and} j_2$) at delay k, respectively. j is the jth type of fault, and n is the total number of different fault categories. $H(I_{kj_1})$ and $H(I_{kj_2})$ are the information entropy of the two images, respectively. $H(I_{kj_1}, I_{kj_2})$ is the joint entropy. The information entropy and joint entropy are calculated as

$$\begin{cases} H(I_{kj_1}) = -\sum_{g_{kj_1}} P_{I_{kj_1}}(g_{kj_1}) \log_2 P_{I_{kj_1}}(g_{kj_1}) I_{kj_2} \\ H(I_{kj_2}) = -\sum_{g_{kj_2}} P_{I_{kj_2}}(g_{kj_2}) \log_2 P_{I_{kj_2}}(g_{kj_2}) \\ H(I_{kj_1}, I_{kj_2}) = -\sum_{g_{kj_1}, g_{kj_2}} P_{I_{kj_1} I_{kj_2}}(g_{kj_1}, g_{kj_2}) \\ \qquad \times \log_2 P_{I_{kj_1} I_{kj_2}}(g_{kj_1}, g_{kj_2}) \end{cases} \tag{4}$$

where g_{kj_1} and g_{kj_2} are the grayscale values of the pixels in the two images, respectively, and their value ranges are between the minimum and maximum grayscale values of the respective images. $P_{I_{kj_1}}(g_{kj_1})$ and $P_{I_{kj_2}}(g_{kj_2})$ are the appearing probability of g_{kj_1} and g_{kj_2}, respectively. $P_{I_{kj_1} I_{kj_2}}(g_{kj_1}, g_{kj_2})$ is the

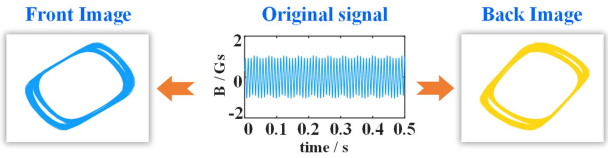

Fig. 3. CDPSR image of normal motor.

joint probability, which represents the ratio of matched pixels in images I_{kj_1} and I_{kj_2} to the total pixels of an image.

Based on d and k, the CDPSR of the fault signal is carried out by the delay reconstruction theorem. For a fault signal $X_1 = (x_{1,1}, x_{1,2}, \ldots, x_{1,N})^T$, the reconstruction can be expressed as [27]

$$\begin{cases} X_1^r = (x_{1,i}, x_{1,i+k}, \ldots, x_{1,i+(d-1)k}) \\ i = 1, 2, \ldots, N-(d-1)\,k \end{cases} \tag{5}$$

where N is the length of the time series. The fault signal is reconstructed as a phase space trajectory. To comprehensively display system characteristics and promote fault diagnosis, the phase space trajectory is given the orientation information of the image based on the visual image knowledge in this article.

The vectors of phase space trajectory are constructed into two images with the same shape and 180° difference in position through the rotation of spatial positions, which are separately defined as front and back CDPSR images.

In this article, the CDPSR images of a normal motor are shown in Fig. 3 ($d = 2, k = 2$). It should be noted that the image color has no specific meaning and is only used to distinguish two images. To reduce the calculation load, the grayscale format of the image is applied in the determination process of k and the fault diagnosis process, and the size of the image is 64×64.

B. Parallel Semisupervised Stacked Autoencoders

To fully utilize the front and back images and mine the information of unlabeled data, this article proposes a PS-SAE model for fault diagnosis based on sparse autoencoders.

1) S-SAEs: As shown in Fig. 2, the front and back CDPSR images converted from the same fault signal are separately input into two parallel S-SAEs for image feature extraction and primary classification. Feature extraction is achieved by stacked sparse autoencoders, whereas primary classification is determined by the softmax classifier. The training process of two S-SAEs can be summarized as follows.

Step 1: Pretraining on Limited Labeled Data. The training goal of the sparse autoencoder is to minimize the loss function, which is utilized to determine the error between the input samples and the decoded reconstructed samples. The loss function is calculated as

$$e = \frac{1}{Q}\sum_{q=1}^{Q}\sum_{c=1}^{C}\left(y_{qc} - \hat{y}_{qc}\right)^2 + \lambda * \Omega_w + \beta * \Omega_s \tag{6}$$

where Q is the total number of training samples and C is the number of neurons in hidden layer. y_{qc} is the$q$th sample input to the encoder, and $\hat{y}_{qc}$is the reconstructed output of the decoder. Ω_w and Ω_s are the L2 regularization and sparsity regularization terms, respectively. λ and β are coefficients.

The stacked structure of multiple autoencoders realizes image feature extraction. By incorporating the image features with data labels to train the softmax classifier. The output of the classifier is the normalized probability of the corresponding fault type, and its calculation can be expressed as

$$P_j(\hat{y}_q) = \frac{e^{\hat{y}_q}}{\sum_{j=1}^{n} e^{\hat{y}_q}} \tag{7}$$

where $\hat{y}_q$ is the feature of the qth input sample extracted by the SAE, and e is the natural logarithm.

Since the training of SAE is unsupervised learning, back-propagation fine-tuning is required to improve the performance of the entire SAE. Fine-tuning is to minimize the loss function of the actual label and the diagnostic label by correcting the SAE parameters. The loss function can be written as

$$\arg\min_{\mathrm{W,b}} \frac{1}{Q}\sum_{q=1}^{Q}\frac{1}{2}\left\|L_q - \hat{L}_q\right\|_2^2 + \frac{\zeta}{2}\sum_{h=1}^{H}\left(\left\|\mathrm{W}^h\right\|_2^2 + \left\|\mathrm{b}^h\right\|_2^2\right) \tag{8}$$

where L_q and $\hat{L}_q$ are the actual label and diagnostic label, respectively. ζ is the tradeoff coefficient of the classification error term and the weight decay term to prevent overfitting of training. H is the number of hidden layers. W^h and b^h are the weights and biases of the neurons in the hth hidden layer, respectively.

Step 2: Semisupervised Learning Based on Unlabeled Data. To enhance the accuracy of the diagnostic model using unlabeled data, this article develops a semisupervised learning strategy. Based on supervised pretraining, unlabeled samples that meet semisupervised conditions are selected for secondary fine-tuning to optimize the model.

An unlabeled training dataset is defined as $\{U\}$. The structural similarity between the unlabeled data image and the labeled data image is chosen as the selection condition. The structural similarity calculation between the unlabeled image (I_U) and the labeled image (I_L) can be expressed as

$$s_m(I_U, I_L) = \frac{(2u_{I_U}u_{I_L} + C_1)(2\sigma_{I_U I_L} + C_2)}{(u_{I_U}^2 + u_{I_L}^2 + C_1)(\sigma_{I_U}^2 + \sigma_{I_L}^2 + C_2)} \tag{9}$$

where u_{I_U}, u_{I_L}, σ_{I_U},σ_{I_L}, and $\sigma_{I_U I_L}$ are the local means, standard deviations, and cross-covariance. C_1 and C_2 are the regularization constants. The unlabeled samples that follow the following conditions are selected for fine-tuning:

$$If(s_m(I_U, I_L) > \alpha)\mathrm{Then}(U_{y_q} \in \{Y\}) \tag{10}$$

where α denotes the determination coefficient, and $\{Y\}$ is the selected unlabeled dataset. The samples in $\{Y\}$ are assigned the same label class as the corresponding labeled data. The pretrained diagnostic model can accurately identify the samples in $\{Y\}$ to a large extent. Therefore, the samples in $\{Y\}$ can be used to fine-tune the overall model.

2) Weighted Decision Layer Fusion Strategy: This article proposes a weighted decision layer fusion method to obtain more accurate and stable diagnosis performance. For n fault

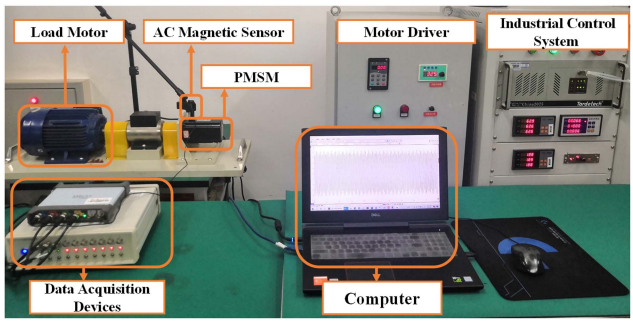

Fig. 4. Experimental platform.

categories, each softmax classifier computes n corresponding primary classification probabilities. The primary classification probabilities of the same sample are fused at the decision level, which can be formulated as

$$P_{UFj} = \frac{1}{2} P_{m1} P_{1j} + \frac{1}{2} P_{m2} P_{2j} \tag{11}$$

where P_{m1} and P_{m2} are the average output probabilities of the two S-SAEs, respectively. P_{1j} and P_{2j} are the probabilities of the input sample belonging to the jth fault class assigned by the two S-SAEs. The final diagnosis result is determined by the "winner takes all" principle, which is given as

$$\text{Fault type} = \arg \max_{j=1,2\cdots n} (P_{UFj}). \tag{12}$$

C. Specific Diagnostic Process

The flowchart of the specific diagnostic process is drawn in Fig. 2, which can be summarized as follows.

Step 1: The magnetic leakage signals are collected and converted into CDPSR images.
Step 2: The CDPSR images are divided into training and test datasets.
Step 3: A few samples in the training dataset are labeled to pretrain PS-SAE.
Step 4: PS-SAE is further fine-tuned by unlabeled samples in the training dataset through semisupervised learning way.
Step 5: The test data is input into the PS-SAE to assess the performance.
Step 6: The trained PS-SAE is used for fault diagnosis.

IV. Case Validation

To demonstrate the effectiveness of the proposed method, an experimental platform was built, and the corresponding verification experiments were carried out.

A. Experimental Platform and Dataset Description

1) Experimental Platform: The experimental platform primarily comprises computers, data acquisition equipment, PMSMs, ac magnetic field sensors, motor drivers, load motors, and industrial control systems, as depicted in Fig. 4. The platform consists of six types of prototypes, specifically a normal motor, a BF, an inter-turn short circuit fault (ISCF), a local demagnetization (LDG), a uniform demagnetization (UDG), and a local magnet damage (LMD). The tabulated parameters of the normal PMSM can be found in Table I. Fault PMSMs are created by implanting faults into normal motors, and the processes for implanting different faults are illustrated in Fig. 5. For BF, the bearing of the PMSM used in this article is deep groove ball bearing, model 6204Z. The BF is implanted by making a small groove point in the inner ring of the bearing. To create the ISCF prototype, a single coil within a phase is short-circuited. To implant early LDG, one of the ten permanent magnets is substituted with a permanent magnet possessing 90% remanence. In contrast, early UDG is attained by replacing all ten permanent magnets with permanent magnets featuring90% remanence. The LMD fault occurs as a result of axial mechanical damage inflicted upon a permanent magnet.

2) Dataset Description: The magnetic leakage signals of PMSMs are captured using the AMS-2K sensor. The signal is collected under multiple working conditions (MWC), encompassing three load conditions (0.00 N·m, 1.63 N·m, and 2.39 N·m) across three speeds (1000 r/min, 1300 r/min, and 1500 r/min). The sampling frequency is 10 kHz. One second of the signal is taken as one sample, and each data class is collected for 120 s. The total sample size of the dataset is $120 \times 3 \times 3 \times 6 = 6480$, 60% of samples are randomly selected as training datasets, and the rest are test datasets. The different speed and load conditions are defined in Table II.

TABLE I
Main Parameters of PMSM

Names	Values	Names	Values
Rated voltage	110 V	Number of poles	10
Rated current	5.1 A	Number of slots	9
Rated torque	2.39 N·m	PM material	NdFe30
Number of phases	3	Magnetization type	Radial
Bearing type	6204Z	Remanence (Br)	1.176 T

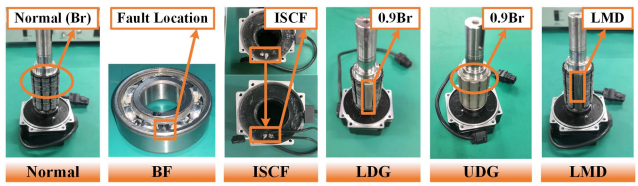

Fig. 5. Processes for implanting different faults.

TABLE II
MWC Description

MWC	Speed	Load
MWC1	1300 r/min	0.00 N·m
MWC2	1300 r/min	1.63 N·m
MWC3	1300 r/min	2.39 N·m
MWC4	1000 r/min	0.00 N·m
MWC5	1500 r/min	0.00 N·m

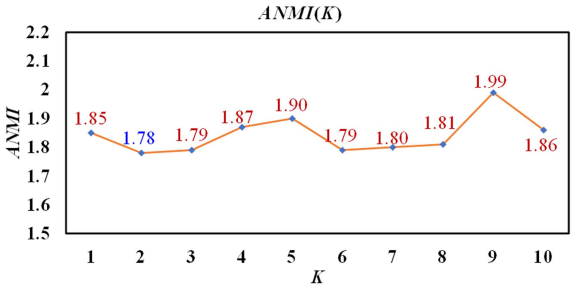

Fig. 6. ANMI among six motors with different k values.

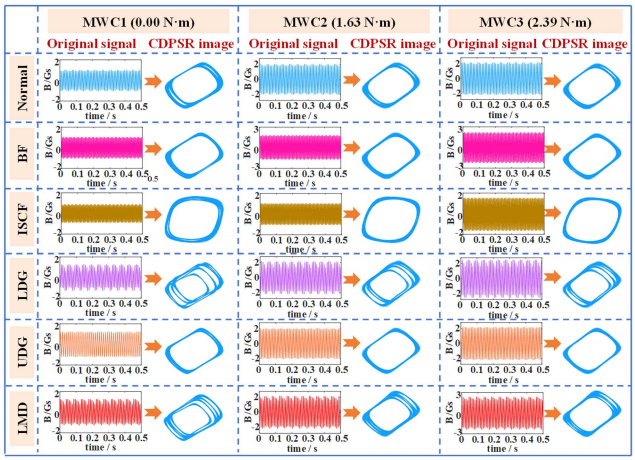

Fig. 7. CDPSR images of different motors.

B. CDPSR Image Analysis

Within the 2-D phase space, k is computed using the magnetic leakage signals obtained during MWC1, through (4) and (5). Fig. 6 shows the ANMI values under different k. It can be observed that $k = 2$ is the first local minimum. For this reason, this article adopts $k = 2$ to reconstruct the magnetic leakage signals into CDPSR images.

The CDPSR images of fault motors are presented in Fig. 7, where the images of fault motors are approximately quadrilateral. There are diversities in the edge thickness, curvature, dispersion, shape, and other features between the different faulty motors and normal motors. For BF, the dispersion of the CDPSR images is small. For the CDPSR images of ISCF, there are obvious changes in curvature. Both LDG and LMD belong to local permanent magnet faults, and their CDPSR images have large dispersion, which changes the shape of the images. The CDPSR images of UDG will be narrower in edge thickness. Under various working conditions, the CDPSR images preserve the similarity of identical faults while capturing the distinctions among different faults. Therefore, the CDPSR image has certain applicability to working conditions, which is more conducive to fault diagnosis than the original signal.

C. Fault Diagnosis and Analysis

Based on the experimental platform, the single working condition experiment and the working condition adaptability experiment are carried out, respectively. In this study, the proposed method and the comparison methods are implemented in the MATLAB R2021b environment. The experiments are conducted on a computer equipped with an Intel Core i7-11800H CPU (2.30 GHz) and 32.00 GB of RAM. All experimental results are the average value of 20 measurements to mitigate contingency, and the standard deviation are listed.

TABLE III
ACCURACY OF SINGLE CONDITION (%)

Methods	2	4	6	8	10	12	14	Mean
SAE1	83.53 ±6.98	85.41 ±6.61	86.37 ±5.51	87.76 ±5.67	89.81 ±5.18	90.81 ±4.98	91.83 ±4.54	87.93 ±5.64
SAE2	82.00 ±7.04	84.98 ±6.92	85.34 ±6.03	86.77 ±5.92	88.68 ±5.09	89.56 ±5.56	90.91 ±5.07	86.89 ±5.99
P-SAE	88.16 ±3.18	90.90 ±3.10	91.08 ±5.72	92.19 ±2.91	92.96 ±3.05	93.51 ±2.69	94.34 ±2.55	91.87 ±3.31
S-SAE1	88.34 ±5.45	91.05 ±5.53	91.89 ±5.61	92.13 ±5.83	93.12 ±5.21	93.75 ±4.33	94.55 ±4.05	92.12 ±5.14
S-SAE2	87.69 ±5.65	90.66 ±5.36	91.79 ±6.09	92.52 ±5.75	92.93 ±4.52	93.16 ±4.42	94.43 ±4.13	91.88 ±5.13
PS-SAE	**90.09 ±2.55**	**93.67 ±2.50**	**94.05 ±1.97**	**94.50 ±1.61**	**95.31 ±1.64**	**96.32 ±1.55**	**97.84 ±1.36**	**94.54 ±2.03**

The number of hidden layers and neurons in SAE is determined by the input data. According to the CDPSR images of the six motors, the parameters of the two S-SAEs in PS-SAE are set the same, where the number of hidden layers is 3, and the corresponding number of neurons is set to 200, 100, and 50 according to the basic decreasing rule. Under different numbers of labeled samples, six methods are implemented and compared, and the experimental results are listed in Table III. The inputs of SAE1 and SAE2 correspond to the front and back CDPSR images, respectively. P-SAE performs decision-level fusion by combining SAE1 and SAE2. These three methods are all supervised learning methods. S-SAE1, S-SAE2, and PS-SAE are the corresponding semisupervised learning methods.

1) Single Working Condition Experiment: Taking the fault diagnosis under MWC1 as an example to carry out the single-condition experiment, and the training dataset and the test dataset belong to the same working condition.

Analysis of semisupervised learning: When the number of labeled samples L ranges from 2 to 14, the semisupervised learning methods have higher accuracy than the supervised learning methods. When $L = 14$, the diagnostic accuracies of S-SAE1, S-SAE2, and PS-SAE are 94.55%, 94.43%, and 97.84%, respectively. While SAE1, SAE2, and P-SAE are 91.83%, 90.91%, and 94.34%, respectively, which are lower than the semisupervised learning methods. Fig. 8 illustrates the confusion matrices of the four methods when the number of labeled samples is 14, where the diagonal line is the number of correctly diagnosed samples, and the last row is the diagnostic accuracy. The yellow grid is the average diagnostic accuracy, i.e., the final diagnostic result output. It can be observed from Fig. 8(a) and (b) that S-SAE1 improves the diagnostic performance of SAE1 in BF and UDG by using unlabeled data. To sum up, the supervised diagnosis model cannot be fully trained when the labeled data is limited, resulting in an unsatisfactory diagnosis effect. Utilizing unlabeled data will effectively improve diagnostic performance through semisupervised learning.

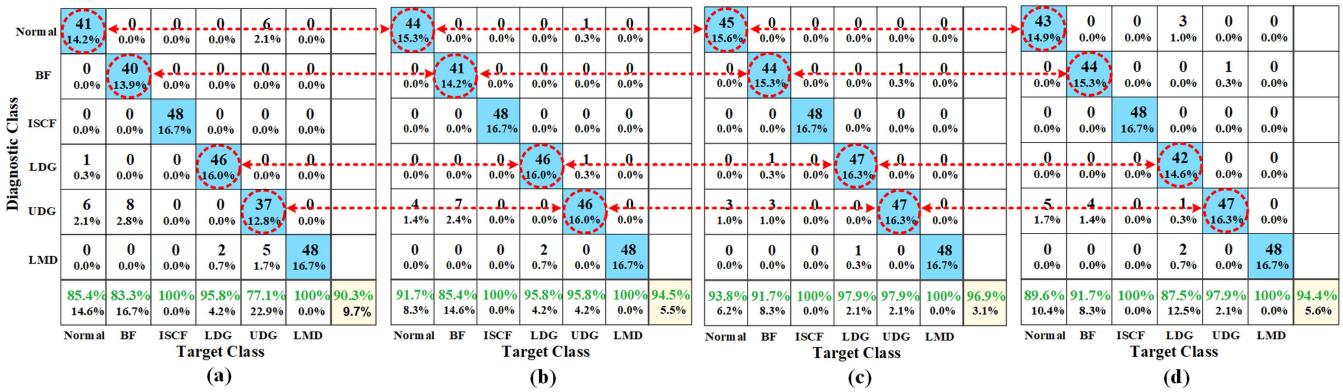

Fig. 8. Confusion matrices. (a) SAE1. (b) S-SAE1. (c) PS-SAE. (d) S-SAE2.

Analysis of decision layer fusion strategy: It can be seen from Table III that P-SAE and PS-SAE have better diagnostic accuracies than the corresponding single SAE. The diagnostic accuracies of PS-SAE in seven different numbers of labeled samples are 90.09%, 93.67%, 94.05%, 94.50%, 95.31%, 96.32%, and 97.84%, whereas the corresponding diagnostic accuracy of S-SAE1 and S-SAE2 are all lower than the above values. Also, the standard deviation values of PS-SAE and P-SAE are lower than single SAE as a whole, which indicates the decision layer fusion strategy can improve the stability of diagnostic results. Fig. 8(b)–(d) demonstrates that PS-SAE enhances the diagnostic accuracy of BF, LDG, and UDG, which is attributed to the proposed decision layer fusion strategy. In summary, the proposed method outperforms the comparison methods in single working conditions.

To fully verify the advantages of PS-SAE, the proposed image-based method is compared with feature extraction methods based on 1-D signals, involving wavelet time scattering (WTS), CWT, and fast Fourier transform (FFT). In WTS, the first filter bank and the second filter bank have 8 wavelets per octave and 1 wavelet per octave, respectively. In CWT, fourth-order autoregressive model coefficients are selected as fault features. In FFT, the peak location, half power bandwidth, peak amplitude, band power, and mean frequency are used as fault features. At the same time, the intelligent methods commonly used in fault diagnosis are used as a supplementary comparison analysis, including support vector machines (SVM) [28], K-nearest neighbor (KNN) [29], decision tree (Tree) [30], image content retrieval-based fault detection (ICR-FD) [31], conditional random field-based graph attention network (CRF-GAT) [32], semisupervised Gaussian random field (SSGRF) [33], semisupervised extreme learning machine (SSELM) [34], and semisupervised deep rule-based (SSDRB) classifier [13] are selected as comparison methods.

To comprehensively evaluate the effectiveness of the proposed method, four indicators namely accuracy, precision, recall, and F1-score are selected [30]. The experiment results of $L = 2$ are shown in Table IV. It is evident that PS-SAE outperforms the comparison methods, demonstrating superior performance across the remaining four indicators. For instance, PS-SAE has a 90.09% accuracy with a standard deviation of 2.55, and the F1-score value is 90.15% with a standard deviation of 2.44.

TABLE IV
ACCURACY OF DIFFERENT COMPARISON METHODS (%)

Methods	Accuracy	Precision	Recall	F1-score
WTS+Tree	49.31±6.31	51.39±6.25	49.31±6.12	50.34±6.04
CWT+SVM	49.75±6.18	54.02±6.14	49.73±6.18	51.85±6.12
FFT+KNN	53.80±7.63	55.82±7.55	53.81±7.84	54.82±7.43
CDPSR+ICR-FD	56.51±4.12	57.21±4.07	55.74±4.72	56.41±4.32
CRF-GAT	85.67±3.33	85.77±3.27	85.71±3.18	85.71±3.19
CDPSR+SSGRF	87.75±4.33	87.80±4.41	87.78±4.35	87.79±4.31
CDPSR+SSELM	88.71±4.57	88.79±4.42	88.77±4.53	88.78±4.32
CDPSR+SSDRB	87.57±3.16	87.45±3.19	87.55±3.21	87.53±3.14
CDPSR+PS-SAE	**90.09±2.55**	**90.12±2.45**	**90.10±2.56**	**90.15±2.44**

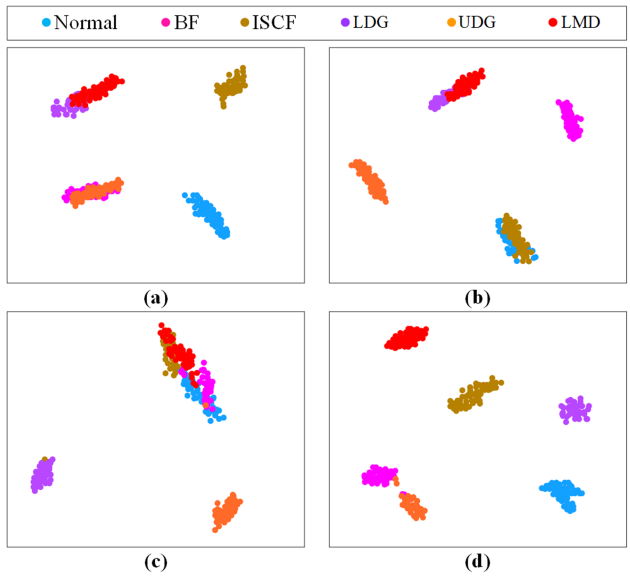

Fig. 9. Feature visualization of different methods. (a) WTS. (b) CWT. (c) FFT. (d) Proposed method.

The t-distributed stochastic neighbor embedding (t-SNE) is applied to examine the feature representations and classification alignments of different methods intuitively [35]. Feature visualization results of different methods are drawn in Fig. 9. It can be observed that features of the same category are well aligned, which explains why the diagnostic accuracy of the proposed method surpasses the contrastive methods in performance.

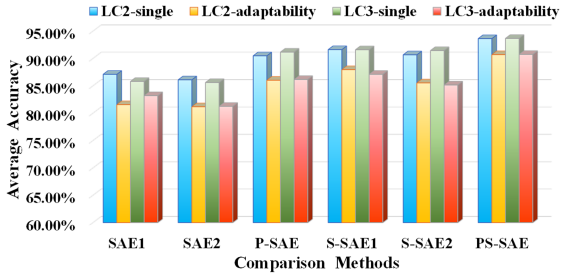

Fig. 10. Comparison of single condition and load adaptability.

TABLE V
ACCURACY OF MWC2-ADAPTABILITY EXPERIMENT (%)

Methods	2	4	6	8	10	12	14	Mean
SAE1	60.30 ±7.75	77.33 ±7.73	85.78 ±7.05	86.69 ±6.75	87.78 ±6.13	89.78 ±5.93	90.85 ±6.32	82.64 ±6.95
SAE2	64.20 ±7.91	76.53 ±7.74	84.44 ±7.79	85.73 ±6.80	87.34 ±6.67	89.53 ±6.97	91.81 ±6.26	82.80 ±7.16
P-SAE	72.12 ±4.48	81.67 ±4.36	89.1 ±4.66	90.38 ±3.12	90.66 ±3.40	93.38 ±3.58	94.15 ±3.37	87.35 ±3.85
S-SAE1	68.92 ±6.71	83.73 ±6.52	87.55 ±6.33	89.70 ±6.17	90.38 ±5.86	92.15 ±5.37	93.48 ±5.46	86.56 ±6.06
S-SAE2	70.53 ±6.32	81.82 ±6.21	86.37 ±6.18	89.25 ±6.01	89.78 ±5.47	92.24 ±5.72	94.11 ±5.53	86.30 ±5.92
PS-SAE	**78.36 ±3.87**	**89.20 ±4.09**	**91.25 ±1.16**	**92.81 ±2.03**	**93.30 ±1.77**	**95.28 ±1.89**	**96.32 ±1.14**	**90.93 ±2.32**

2) Adaptation Experiments Under Different Load: To verify the load adaptability of the proposed method, the trained diagnostic model in MWC1 is fine-tuned in MWC2 and MWC3 for fault diagnosis of these two working conditions. The average diagnostic accuracies in the single working condition experiment and load adaptability experiment are presented in Fig. 10. The results under MWC2 are listed in Table V.

Table V illustrates that when a few labeled training samples are implemented, the diagnostic model is greatly affected by the working conditions. When $L = 2$, the diagnostic accuracy of PS-SAE is 78.36%, which is about 12% lower than the single working condition. With the increase of labeled samples, the diagnostic accuracy is greatly improved with the promotion of the CDPSR image similarity and fine-tuning between different working conditions. When $L = 14$, PS-SAE achieves the best accuracy of 96.32%. Fig. 10 shows that all methods are affected by working conditions, but the proposed method suffers the least impact and has the best average diagnostic result (90.93%), which exhibits great promise to solve load adaptability.

3) Adaptation Experiments Under Different Speeds: In this section, the practicability of the proposed method at low speed, medium speed, and high speed are further analyzed. The diagnostic model trained by MWC1 is fine-tuned by MWC4, and MWC5 for the fault diagnosis of these two working conditions, respectively. The CDPSR images of three speeds under no-load conditions are shown in Fig. 11 (front image). The experimental results under MWC4 *are* separately shown in Table VI.

In Fig. 11, it is obvious that the same features of the identical fault and the different features between faults are still well preserved. Table VI illustrates that PS-SAE has higher diagnostic

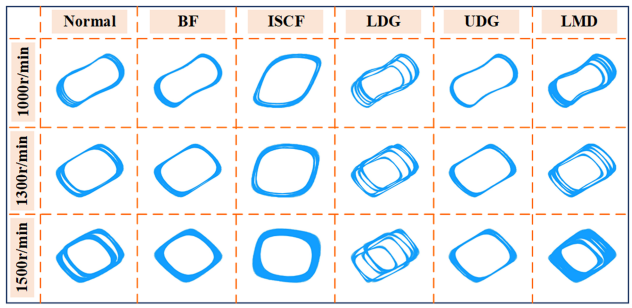

Fig. 11. CDPSR images of different speeds under no-load conditions.

TABLE VI
ACCURACY OF MWC4-ADAPTABILITY EXPERIMENT (%)

Methods	2	4	6	8	10	12	14
SAE1	45.75 ±8.31	56.45 ±7.83	63.36 ±7.86	68.49 7.79	74.52 ±7.36	79.24 ±7.72	82.60 ±6.81
SAE2	42.77 ±8.42	55.81 ±8.37	62.40 ±7.42	66.61 ±7.83	75.36 ±7.50	79.57 ±7.69	83.79 ±7.07
P-SAE	55.62 ±5.78	61.32 ±5.62	66.18 ±5.24	72.5 ±4.66	77.71 ±4.51	83.23 ±4.13	89.69 ±3.39
S-SAE1	51.55 ±7.63	63.85 ±7.75	69.03 ±7.41	74.24 ±7.52	79.55 ±7.11	82.81 ±6.79	88.63 ±6.26
S-SAE2	54.37 ±7.80	60.51 ±7.69	68.21 ±7.61	75.48 ±7.47	83.27 ±7.26	86.53 ±6.55	89.92 ±6.38
PS-SAE	**61.42 ±4.82**	**85.33 ±4.75**	**87.08 ±3.47**	**90.92 ±3.75**	**91.29 ±3.18**	**92.31 ±2.63**	**94.18 ±2.34**

accuracy than the contrastive methods under different speed conditions. Table VI shows that when $L = 14$, PS- SAE achieves the best accuracy of 94.18%, which is about 4.26% higher than the S-SAE2. The experiment results verify the effectiveness of PS-SAE in tackling speed adaptability.

V. CONCLUSION

To utilize the neglected 2-D fault features of signal and achieve accurate fault diagnosis under few-labeled samples, an intelligent diagnosis method for PMSM based on CDPSR images and two-parallel diagnosis architecture was proposed in this article. Different from most methods of signal analysis, the proposed method reconstructed the 1-D magnetic leakage signal into a CDPSR image as the input of the diagnostic model, which reduced the complexity of fault diagnosis and improved the accuracy. The two-parallel diagnosis architecture with the decision layer fusion strategy fully exploited the information of unlabeled data through a semisupervised learning way, which improved diagnostic robustness.

The proposed method was verified on an experimental platform for PMSM. In the single working condition experiment, a diagnostic accuracy of 90.09% was achieved with only two labeled samples, whereas a diagnostic accuracy of 97.84% was achieved with 14 labeled samples. In the MWC adaptation experiments, diagnostic accuracies of 96.32% and 94.18% were achieved for the load adaptability experiment and speed adaptability experiment, respectively, with 14 labeled samples. The experimental results demonstrated the efficacy of the proposed

method in fault diagnosis of PMSM, along with a certain degree of adaptability to diverse working conditions.

Future studies will be carried out on multidimensional reconstruction and fusion technology under 1-D signal, fault prediction, and accurate positioning technology of PMSM.

REFERENCES

[1] J. Gao, W. Gui, C. Yang, T. Peng, J. Luo, and Y. Han, "Multiple observers-based demagnetization fault detection with inductance mismatch impacts eliminated for PMSMs," *IEEE Trans. Power Electron.*, vol. 38, no. 7, pp. 8016–8021, Jul. 2023.

[2] A. Moradzadeh, B. Mohammadi-Ivatloo, K. Pourhossein, and A. A. Moghaddam, "Data mining applications to fault diagnosis in power electronic systems: A systematic review," *IEEE Trans. Power Electron.*, vol. 37, no. 5, pp. 6026–6050, May 2022.

[3] Y. Chen, D. Zhang, H. Zhang, and Q.-G. Wang, "Dual-path mixed domain residual threshold networks for bearing fault diagnosis," *IEEE Trans. Ind. Electron.*, vol. 69, no. 12, pp. 13462–13472, Dec. 2022.

[4] X. Song, J. Zhao, J. Song, F. Dong, L. Xu, and J. Zhao, "Local demagnetization fault recognition of permanent magnet synchronous linear motor based on S-transform and PSO–LSSVM," *IEEE Trans. Power Electron.*, vol. 35, no. 8, pp. 7816–7825, Aug. 2020.

[5] H. Chen, C. Gao, J. Si, Y. Nie, and Y. Hu, "A novel method for diagnosing demagnetization fault in PMSM using toroidal-yoke-type search coil," *IEEE Trans. Instrum. Meas.*, vol. 71, 2022, Art. no. 7501012.

[6] Q. Song, M. Wang, W. Lai, and S. Zhao, "On Bayesian optimization-based residual CNN for estimation of inter-turn short circuit fault in PMSM," *IEEE Trans. Power Electron.*, vol. 38, no. 2, pp. 2456–2468, Feb. 2023.

[7] B. Cai, Y. Zhao, H. Liu, and M. Xie, "A data-driven fault diagnosis methodology in three-phase inverters for PMSM drive systems," *IEEE Trans. Power Electron.*, vol. 32, no. 7, pp. 5590–5600, Jul. 2017.

[8] J. Song et al., "Accurate demagnetization faults detection of dual-sided permanent magnet linear motor using enveloping and time-domain energy analysis," *IEEE Trans. Ind. Inform.*, vol. 16, no. 10, pp. 6334–6346, Oct. 2020.

[9] E. Ghosh, A. Mollaeian, S. Kim, J. Tjong, and N. C. Kar, "DNN-based predictive magnetic flux reference for harmonic compensation control in magnetically unbalanced induction motor," *IEEE Trans. Magn.*, vol. 53, no. 11, Nov. 2017, Art. no. 8210907.

[10] W. Cao et al., "Analysis of inter-turn short-circuit faults in brushless DC motors based on magnetic leakage flux and back propagation neural network," *IEEE Trans. Energy Convers.*, early access, Jun. 21, 2023, doi: 10.1109/TEC.2023.3285899.

[11] Y. Wang, M. Yang, Y. Li, Z. Xu, J. Wang, and X. Fang, "A multi-input and multi-task convolutional neural network for fault diagnosis based on bearing vibration signal," *IEEE Sens. J.*, vol. 21, no. 9, pp. 10946–10956, May 2021.

[12] E. T. Esfahani, S. Wang, and V. Sundararajan, "Multisensor wireless system for eccentricity and bearing fault detection in induction motors," *IEEE/ASME Trans. Mechatron.*, vol. 19, no. 3, pp. 818–826, Jun. 2014.

[13] F. Huang et al., "Demagnetization fault diagnosis of permanent magnet synchronous motors using magnetic leakage signals," *IEEE Trans. Ind. Inform.*, vol. 19, no. 4, pp. 6105–6116, Apr. 2023.

[14] A. Choudhary, D. Goyal, and S. S. Letha, "Infrared thermography-based fault diagnosis of induction motor bearings using machine learning," *IEEE Sens. J.*, vol. 21, no. 2, pp. 1727–1734, Jan. 2021.

[15] X. Li, H. Shao, S. Lu, J. Xiang, and B. Cai, "Highly efficient fault diagnosis of rotating machinery under time-varying speeds using lsismm and small infrared thermal images," *IEEE Trans. Syst. Man Cybern. Syst.*, vol. 52, no. 12, pp. 7328–7340, Dec. 2022.

[16] M.-Q. Tran, M.-K. Liu, Q.-V. Tran, and T.-K. Nguyen, "Effective fault diagnosis based on wavelet and convolutional attention neural network for induction motors," *IEEE Trans. Instrum. Meas.*, vol. 71, 2022, Art. no. 3501613.

[17] F. Huang et al., "Multisource unsupervised subdomain adaptation network for rotary machine fault diagnosis," *IEEE Trans. Instrum. Meas.*, vol. 72, 2023, Art. no. 3510611.

[18] J.-M. Huang, R.-J. Wai, and G.-J. Yang, "Design of hybrid artificial bee colony algorithm and semi-supervised extreme learning machine for PV fault diagnoses by considering dust impact," *IEEE Trans. Power Electron.*, vol. 35, no. 7, pp. 7086–7099, Jul. 2020.

[19] S. Zheng and J. Zhao, "A self-adaptive temporal-spatial self-training algorithm for semi-supervised fault diagnosis of industrial processes," *IEEE Trans. Ind. Inform.*, vol. 18, no. 10, pp. 6700–6711, Oct. 2022.

[20] X. Zhang, Z. Su, X. Hu, Y. Han, and S. Wang, "Semi-supervised momentum prototype network for gearbox fault diagnosis under limited labeled samples," *IEEE Trans. Ind. Inform.*, vol. 18, no. 9, pp. 6203–6213, Sep. 2022.

[21] Y. Zhang, Z. Ren, and S. Zhou, "An intelligent fault diagnosis for rolling bearing based on adversarial semi-supervised method," *IEEE Access*, vol. 8, pp. 149868–149877, 2020.

[22] X. Nie and G. Xie, "A two-stage semi-supervised learning framework for fault diagnosis of rotating machinery," *IEEE Trans. Instrum. Meas.*, vol. 70, 2021, Art. no. 3521212.

[23] J. Liu et al., "Toward robust fault identification of complex industrial processes using stacked sparse-denoising autoencoder with softmax classifier," *IEEE Trans. Cybern.*, vol. 53, no. 1, pp. 428–442, Jan. 2023.

[24] T. Wang, Z. Zhang, and K.-L. Tsui, "A deep generative approach for rail foreign object detections via semi-supervised learning," *IEEE Trans. Ind. Inform.*, vol. 19, no. 1, pp. 459–468, Jan. 2023.

[25] S. Wang, H. Shuai, and Q. Liu, "Phase space reconstruction driven spatio-temporal feature learning for dynamic facial expression recognition," *IEEE Trans. Affect. Comput.*, vol. 13, no. 3, pp. 1466–1476, Jul.–Sep. 2022.

[26] J. Xie, Z. Long, X. Zhang, G. Qin, F. Huang, and Z. Rao, "Demagnetization fault diagnosis of PMSM using custom phase space reconstruction image," *IEEE Trans. Instrum. Meas.*, vol. 72, 2023, Art. no. 3526211.

[27] G. Li, Y. Li, and F. Roozitalab, "Midterm load forecasting: A multistep approach based on phase space reconstruction and support vector machine," *IEEE Syst. J.*, vol. 14, no. 4, pp. 4967–4977, Dec. 2020.

[28] B. Brusamarello, J. C. C. da Silva, K. de Morais Sousa, and G. A. Guarneri, "Bearing fault detection in three-phase induction motors using support vector machine and fiber Bragg grating," *IEEE Sens. J.*, vol. 23, no. 5, pp. 4413–4421, Mar. 2023.

[29] M. Shi, R. Zhao, Y. Wu, and T. He, "Fault diagnosis of rotor based on local-global balanced orthogonal discriminant projection," *Measurement*, vol. 168, Jan. 2021, Art. no. 108320.

[30] G. H. Bazan, P. R. Scalassara, W. Endo, A. Goedtel, R. H. C. Palácios, and W. F. Godoy, "Stator short-circuit diagnosis in induction motors using mutual information and intelligent systems," *IEEE Trans. Ind. Electron.*, vol. 66, no. 4, pp. 3237–3246, Apr. 2019.

[31] J. Xie et al., "Fault detection of permanent magnet synchronous motor based on image content retrieval," *IEEE Trans. Instrum. Meas.*, vol. 71, 2022, Art. no. 3530010.

[32] Y. Tang et al., "Rotating machine systems fault diagnosis using semisupervised conditional random field-based graph attention network," *IEEE Trans. Instrum. Meas.*, vol. 70, 2021, Art. no. 3521010.

[33] S. M. K. Zaman, X. Liang, and L. Zhang, "Greedy-gradient max cut-based fault diagnosis for direct online induction motors," *IEEE Access*, vol. 8, pp. 177851–177862, 2020.

[34] G. Huang, S. Song, J. N. D. Gupta, and C. Wu, "Semi-supervised and unsupervised extreme learning machines," *IEEE Trans. Cybern.*, vol. 44, no. 12, pp. 2405–2417, Dec. 2014.

[35] Y. Tang et al., "Multi-sensor-driven motor fault diagnosis method based on visual features," *IEEE Trans. Ind. Inform.*, vol. 19, no. 4, pp. 5902–5914, Apr. 2023.

[36] S. Yu, M. Wang, S. Pang, L. Song, and S. Qiao, "Intelligent fault diagnosis and visual interpretability of rotating machinery based on residual neural network," *Measurement*, vol. 196, Apr. 2022, Art. no. 111228.

Jinping Xie received the B.S. degree in communication engineering from Hunan Institute of Science and Technology, Yueyang, China, in 2015, and the M.S. degree in computer applications technology from Wenzhou University, Wenzhou, China, in 2018. He is currently working toward the Ph.D. degree in electrical engineering with the College of Electrical and Information Engineering, Hunan University, Changsha, China.

His research interests include wind energy conversion systems, predictive current control, and permanent magnet synchronous motor fault diagnosis.

Xiaofei Zhang (Senior Member, IEEE) was born in 1983. He received the M.S. and Ph.D. degrees in mechanical engineering from Science and Technology on Integrated Logistics Support Laboratory, National University of Defense Technology, Changsha, China, in 2006 and 2013, respectively.

From 2013 to 2018, he was a Lecturer with the National University of Defense Technology. Since 2018, he has been an Associate Professor with the College of Electrical and Information Engineering, Hunan University, Changsha. He has chaired more than 20 projects including NSFC. He has authored or coauthored more than 30 academic papers published in journals. His research interests include condition monitoring, fault diagnostics, prognostics, and health management.

Derong Luo was born in Hunan, China, in 1968. He received the B.S. degree in electrical engineering from Harbin University of Science and Technology, Harbin, China, in 1990, and the M.S. and Ph.D. degrees in electrical engineering from Hunan University, Changsha, China, in 1993 and 2013, respectively.

He is currently a Professor with the College of Electrical and Information Engineering, Hunan University. His research interests include wind energy conversion systems, generator design and control, and electronic systems and control.

Guojun Qin was born in 1970. He received the B.Sc. degree in instrument science and technology and the Ph.D. degree in mechanical engineering from the National University of Defense Technology, Changsha, China, in 1992 and 1998, respectively.

He is currently a Professor with Hunan University, Changsha, China. He has chaired more than ten projects, including NSFC 863 Project. He has authored or coauthored more than 60 academic papers in several reputed journals. His research interests include condition monitoring and fault diagnostics, prognostics and health management, and Internet of Things.

Fengqin Huang received the B.S. degree in automation from Lanzhou Jiaotong University, Lanzhou, China, in 2018. She is currently working toward the Ph.D. degree in electrical engineering with the College of Electrical and Information Engineering, Hunan University, Changsha, China.

Her research interests include fault diagnosis, fault information visualization, wind energy conversion systems, and fault-tolerant control.